Nanoscale

PAPER

Check for updates

Charge carrier recombination processes, intragap defect states, and photoluminescence mechanisms in stoichiometric and reduced TiO$_2$ brookite nanorods: an interpretation scheme through *in situ* photoluminescence excitation spectroscopy in controlled environment†

Romina Rega,‡[a] Ambra Fioravanti,‡[b] S. M. Hossein Hejazi,[c,d] Mahdi Shahrezaei,[c] Štěpán Kment,[c,d] Pasqualino Maddalena, [ID][e] Alberto Naldoni [ID] *[f] and Stefano Lettieri [ID] *[e]

The study of titanium dioxide (TiO$_2$) in the brookite phase is gaining popularity as evidence has shown the efficient photocatalytic performance of this less investigated polymorph. It has been recently reported that defective anisotropic brookite TiO$_2$ nanorods display remarkable substrate-specific reactivity towards alcohol photoreforming, with rates of hydrogen production significantly (18-fold) higher than those exhibited by anatase TiO$_2$ nanoparticles. To elucidate the basic photo-physical mechanisms and peculiarities leading to such an improvement in the photoactive efficiency, we investigated the recombination processes of photo-excited charge carriers in both stoichiometric and reduced brookite nanorods *via* photoluminescence excitation spectroscopy in controlled environment. Through an investigation procedure employing both supragap and subgap excitation during successive exposure to oxidizing and reducing gaseous agents, we firstly obtained an interpretation scheme describing the main photoluminescence and charge recombination pathways in stoichiometric and reduced brookite, which includes information about the spatial and energetic position of the intragap states involved in photoluminescence mechanisms, and secondly identified a specific photoluminescence enhancement process occurring in only reduced brookite nanorods, which indicates the injection of a conduction band electron during ethanol photo-oxidation. The latter finding may shed light on the empirical evidence about the exceptional reactivity of reduced brookite nanorods toward the photo-oxidation of alcohols and the concomitant efficiency of photocatalytic hydrogen generation.

[a]*Institute of Applied Sciences and Intelligent Systems "Eduardo Caianiello", National Research Council (CNR-ISASI), Via Cintia 21, 80126 Napoli, Italy*
[b]*Institute of Sciences and Technologies for Sustainable Energy and Mobility, National Research Council (CNR-STEMS), Via Canal Bianco 28, 44124 Ferrara, Italy*
[c]*Czech Advanced Technology and Research Institute, Regional Centre of Advanced Technologies and Materials, Palacký University Olomouc, Křížkovského 511/8, 77900 Olomouc, Czech Republic*
[d]*Nanotechnology Centre, Centre for Energy and Environmental Technologies, VŠB–Technical University of Ostrava, 17. listopadu 2172/15, Poruba, 708 00 Ostrava, Czech Republic*
[e]*Department of Physics "E. Pancini", University of Naples Federico II, Complesso Universitario di Monte S. Angelo, Via Cintia 21 80126 Napoli, Italy.*
E-mail: stefano.lettieri@unina.it
[f]*Department of Chemistry, University of Turin, Via Pietro Giuria, 7, 10125 Torino, Italy. E-mail: alberto.naldoni@unito.it*
†Electronic supplementary information (ESI) available: XRD spectra as-synthesized brookite nanorods; PLE maps and excitation spectra for B700-1 h samples; study of higher-energy ("green") *vs.* lower-energy ("red") spectral components of the visible PL of B700-2 h. See DOI: https://doi.org/10.1039/d4nr00593g
‡These authors contributed equally to this work.

1. Introduction

It is well known that many solids can exist in different crystalline structures, called polymorphs, which exhibit distinct differences in surface atom arrangements and surface energies. Hence, the existence of polymorphs is very significant in fields where the surface properties of a material play a leading role, such as photocatalysis[1] and chemical sensing.[2] Among polymorphic metal oxides, titanium dioxide (TiO$_2$) stands as an important material for chemical sensing[3] and the most widely studied photocatalyst. It has four known polymorphs: rutile (the most thermodynamically stable phase, a tetragonal system, space group $P4_2/mnm$, and number 136), anatase (a tetragonal system, space group $I4_1/amd$, and number 141), brookite (an orthorhombic system, space group $Pbca$, and number 61) and bronze TiO$_2$(B) (a monoclinic system, space group $C2/m$, and number 12).

Among them, the first two are employed in numerous scientific papers and applications.

Brookite TiO_2 is significantly less investigated than rutile and anatase, mainly, because its synthesis in pure form is comparatively difficult to achieve. Earlier studies on brookite TiO_2 synthesis date back to the 1950s.[4] Since then, and specifically in the last decade, significant advancements have been made towards the synthesis of brookite TiO_2 nanoparticles and films[5,6] and towards the controlled growth of TiO_2 crystals in a pure or mixed phase.[7] Owing to such synthesis improvements, the photocatalytic performances of brookite TiO_2 have been increasingly tested, and in recent years, brookite is gaining popularity considering the scientific works reporting the efficient photocatalytic performances of this polymorph, in many cases even showing better results than the more commonly used rutile and anatase polymorphs.[1,8–14] In addition to the specific photoactive properties of pure brookite, it is also worth noting that mixed phase TiO_2, in which brookite is compounded with rutile and/or anatase, can also be extremely useful. These systems are usually highly photoactive[8] because heterojunctions present at the border regions between distinct phases can enhance the separation of photogenerated electron–hole pairs, hindering their recombination.[7]

The use of appropriate co-catalysts,[15,16] engineering of a TiO_2 photocatalyst in photonic crystal structures,[17,18] single-atom catalysts[19,20] and reduction through hydrogenation or other means[21–23] are currently regarded as promising options for extending the application potential of TiO_2. Regarding the latter route, a recent work by Hejazi and coworkers[24] demonstrated the possibility of designing an efficient photocatalyst consisting of defective anisotropic brookite TiO_2 nanorods (NRs) characterized by engineered defectivity obtained through reductive thermal treatments in H_2. Upon platinization, the photocatalyst displayed a substrate-specific boosted reactivity towards alcohol photoreforming compared to the case of anatase and brookite with isotropic nanocrystals. Notably, an increase in the rate of hydrogen evolution up to 18-fold higher than that of the pure anatase TiO_2 counterpart was evidenced during methanol photoreforming.

Elucidating the mechanisms governing the fate of photogenerated charge carriers in the photocatalyst is of primary importance to advance our understanding of photocatalytic performances and how to tailor them. In this regard, employing photoluminescence (PL) spectroscopy is especially useful, particularly for the study of indirect bandgap semiconductors, such as TiO_2. In fact, PL occurs *via* the radiative recombination of a photogenerated electron–hole pair, which in any indirect semiconductor can happen *via* only the spatial superposition of a free charge carrier with a trapped charge carrier. Hence, their PL efficiency depends on the location of defects that trap the charge carriers by the mobility of photogenerated electrons and/or holes and by the possible occurrence of charge-depleted layers below the surface of the material induced by chemisorbed species. In other words, the PL activity of an indirect semiconductor is controlled by structural defectivity and surface properties. This explains why in many instances PL spectroscopy is demonstrated to be a sensitive tool for the analysis of metal oxides; few

examples include *in situ* analysis of redox reactions,[25] optochemical sensing[26] and probing residual surficial presence of anatase in anatase-to-rutile conversion.[27]

As the structural defectivity also decisively defines the photocatalytic properties, the correlations between them and the PL characteristics are evident, establishing PL as a powerful tool to analyze the behavior of photogenerated charges in photocatalysts.[28–31] However, it is important to highlight that PL studies can be conducted at various levels of sophistication. Routine PL analyses based on simple and stand-alone setups are often insufficient to provide basic information; for example, the chemical nature of the defect involved in the observed charge recombination. Further information can be extracted by probing the PL processes activated by variable excitation wavelengths, a procedure known as "excitation-resolved" PL spectroscopy (shortened as PLE), which can, for example, probe the formation of structural defects[32] and/or other PL-active states related to sample modifications.[33–35]

Through the analysis of the PLE data, we derive and present an interpretation scheme describing the leading charge recombination processes and photoluminescence mechanisms in stoichiometric and reduced brookite TiO_2 nanorods. To achieve this, we used a specific PLE procedure employing (a) optical excitation of the photocatalysts at both sub-bandgap and supra-bandgap wavelengths and (b) ambient controlled (*in situ*) measurements, supplying reducing and oxidizing agents in gaseous form at controlled flow rates and low concentrations. As we discussed, these elements carry several advantages over studying the catalyst PL in a liquid environment (*e.g.*, in contact with solvents) and, more importantly, are necessary to extract basic information about the recombination processes.

Our analysis identifies two leading charge recombination pathways: (i) recombination of free and shallowly-trapped electrons recombining with trapped holes, which we interpreted as the origin of visible light emission in the 500–700 nm range, and (ii) recombination of non-photogenerated and deeply-trapped electrons with free holes occurring at the nanorod surface, which originates from the near-infrared light emission centered at 830 nm.

Additionally, (iii) we evidenced a substrate-specific process that occurs during the interaction of reduced brookite with ethanol under ultraviolet illumination and causes a large enhancement of visible PL at supragap excitation. Based on our model, we interpret this phenomenon as being caused by the injection of free electrons in the conduction band of reduced brookite NRs during the initial photo-oxidation of ethanol. Such a specific effect may shed light on the empirical evidence reported regarding their exceptional reactivity toward the photo-oxidation/reforming of alcohols.

2. Experimental details

2.1. Preparation of brookite nanorods and sample nomenclature

Anisotropic brookite nanostructures (nanorods, NRs for brevity) were prepared for the present study using a hydro-

thermal method. Titanium(IV) bis(ammonium lactate) dihydroxide $[NH_4C_3H_4O_3]_2Ti(OH)_2$ in a 50 wt% aqueous solution (obtained from Sigma–Aldrich) referred to as TALH, along with an 11.5 M urea solution in deionized (DI) water, which was of ACS reagent quality (also provided by Sigma–Aldrich), were used as precursors. The process followed a hydrothermal method, which was previously detailed elsewhere.[24]

To initiate the synthesis, 1 mL of TALH was combined with 9 mL of urea in DI water and stirred until a clear solution was achieved. This solution was then transferred to a 25 mL Teflon-lined autoclave, which was subsequently placed in an oil bath set at 180 °C. During this time, the mixture was stirred at 800 rpm for 6 days. Following this hydrothermal treatment, the autoclave was allowed to cool at an ambient temperature. The resulting precipitate was then subjected to multiple cycles of separation through centrifugation and sonication in DI water until the pH of the supernatant reached a neutral level. In the last step, the obtained precipitate was dried in a freeze dryer for 24 h.

The as-synthesized powders, from here onwards referred to as B-AS, exhibited a white appearance in conformity with the diffused reflectance data shown in Fig. 1. Reduced brookite NRs were successively prepared by thermal treatment under a hydrogen (H_2) stream at different temperatures. No significant amounts of non-metal contaminants were detected *via* the

CHN analysis of the as-synthesized and reduced samples.[24] The data presented in this work involve samples of stoichiometric TiO_2 brookite (B-AS) and reduced brookite subjected to reduction treatment in H_2 at a temperature of 700 °C for time durations of 1 hour and 2 hours. The nomenclature used for the reduced samples first indicates the reduction temperature and then the treatment duration. For example, the abbreviation B700-2 h is used here to indicate the sample consisting of nanorods reduced at 700 °C for 2 hours.

2.2. Structural, morphological, and optical characterizations

X-ray diffraction (XRD) patterns were recorded at room temperature (26 °C) using an Empyrean (PANalytical, Almelo, the Netherlands) diffractometer in Bragg–Brentano geometry with Co-Kα radiation (40 kV, 30 mA, $\lambda = 0.1789$ nm). The diffractometer was equipped with a PIXcel3D detector, programmable divergence and diffracted beam anti-scatter slits. The measurement range was $2\theta = 10°–100°$, with a step size of 0.0167° and an acquisition time of 4 s per step.

The morphological analyses of the samples were performed by transmission electron microscopy (TEM) JEM-2100 (JEOL, Tokyo, Japan) at an accelerating voltage of 200 kV. For TEM measurements, the samples were dispersed in ethanol by sonication for 5 minutes; then, the suspensions were dropped on
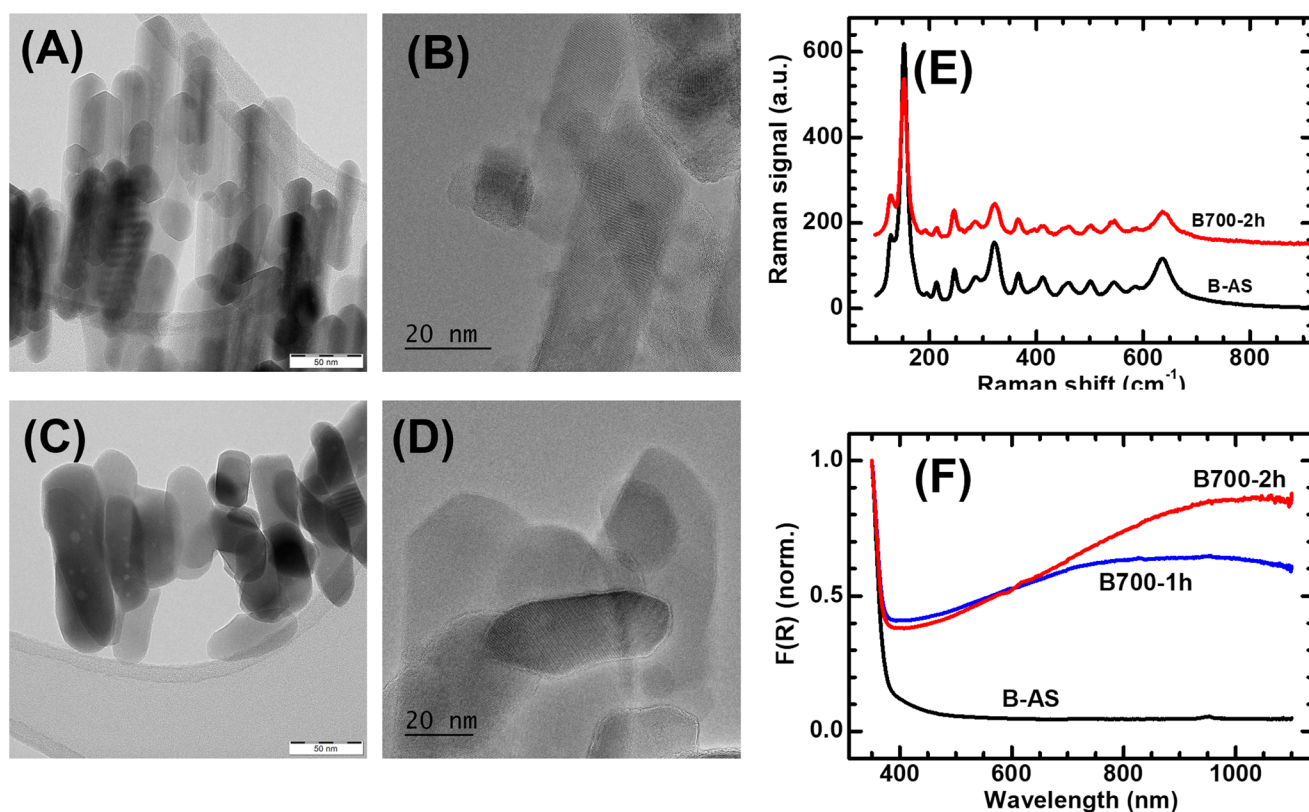

Fig. 1 (A and B) TEM and HRTEM images of the B-AS sample. (C and D) TEM and HRTEM images of the B700-2 h sample. (E) Raman spectra of B-AS (black curve) and B700-2 h (red curve). (F) Peak-normalized Kubelka–Munk function $F(\lambda)$ obtained from the diffused reflectance spectra $R(\lambda)$ measured of the B-AS (black curve), B700-1 h (blue curve) and B700-2 h (red curve) samples.

the copper grid with holey carbon film and dried upon air exposure.

Raman spectra were collected using a DXR Raman spectrometer (Thermo Scientific, Massachusetts, USA). The excitation laser was operated at a wavelength of 455 nm. The samples were deposited on a silicon wafer, and the laser was focused on its surface and tuned to maximize the signal. The laser power on the sample was set to 0.1 mW cm^{-2}, and the exposure time was 3 s.

The ultraviolet-visible diffuse reflectance spectra of the samples were measured using a Specord 250 Plus (Analytik Jena, Jena, Germany) spectrophotometer. An integrating sphere was used to collect the spectrum, and a Spectralon reference sample was used to measure the background.

2.3. PLE spectroscopy in controlled environment

2.3.1. Rationale and definitions. PL measurements at the variable excitation wavelength, hereinafter also referred to as excitation-resolved PL or, more simply, PLE (photoluminescence excitation) spectroscopy, were conducted as the main tool for studying the pathways of charge-carrier recombination in the brookite nanorods by analyzing how the various radiative recombination processes are modified by the interaction of the oxidizing and reducing gaseous species with the charge carriers.

It is important to highlight that carrying out the analyses in a controlled gaseous environment instead of using liquid solvents has the following specific advantages.

(1) Employing a gaseous environment instead of liquids to investigate redox-induced PL changes allows for avoiding alterations in the optical absorption of the catalyst and in the optical path of emitted light, which can affect, in non-controllable ways, the light collection and hence the measured PL intensity.

(2) Using controlled and low concentrations of the redox species avoids the saturation of the PL response that usually occurs at high concentration values of the adsorbed species, which often occurs when the catalyst is in contact with liquid solvents.

(3) The use of pure gas flows instead of the aqueous solution of the analyte avoids humidity, which usually acts as an interfering species and yields cross-interactions that complicate the interpretation of the data.

(4) Supplying the redox molecule at a constant rate allows precise monitoring of the time dynamics of the catalyst–molecule interaction.

Molecular nitrogen (N_2) and oxygen (O_2) were used here as inert and oxidizing species, respectively, while ethanol (EtOH) diluted at 100 ppm concentration in N_2 was employed as the reducing species. The choice of ethanol was consistent with the goal of deepening our understanding of the interaction between alcohols and brookite NR photocatalysts, given the applicative relevance of the investigated materials for alcohol photoreforming.

By "PLE maps", we henceforth mean the contour plots of the quantities $\Phi(\lambda_{PL}\lambda_{exc})$, which designate the intensity (in cps units) of the PL intensity measured at wavelength λ_{PL} when the sample is excited by light of wavelength λ_{exc}.

The term "PLE spectra" indicates the total intensity of PL radiation emitted at a specified interval $\Delta\lambda_{PL}$ of emission wavelengths. They are indicated by $I_{PLE}(\lambda_{exc}\Delta\lambda_{PL})$, which is defined as follows:

$$I_{PLE}(\lambda_{exc}, \Delta\lambda_{PL}) = \int_{\Delta\lambda_{PL}} \Phi(\lambda_{PL}, \lambda_{exc})d\lambda_{PL}. \quad (1)$$

The experimental PLE spectra are obtained *via* the numerical integration of the PLE maps over the selected interval $\Delta\lambda_{PL}$.

The optical excitation wavelength in the PLE experiments for B-AS varied in the interval $\Delta\lambda_{exc}$ = 350–470 nm, corresponding to photon energy interval 3.54–2.64 eV. In the case of reduced (B700) samples, a narrower interval of $\Delta\lambda_{exc}$ = 350–470 nm (photon energy 3.54–2.82 eV) was employed because no significant PL signal was detectable at a wavelength longer than 440 nm.

2.3.2. Experimental setup. PLE spectroscopy in controlled environment was conducted using a white-light Xe lamp (450 W power) optically coupled with a computer-controlled monochromator equipped with two diffraction gratings with a groove density of 1200 grooves per mm. This system provided a tunable light excitation beam spectrally narrowed to an FWHM of about $\Delta\lambda \approx 2$ nm that was collected *via* a liquid-core flexible waveguide and slightly focused on the sample plane to obtain a circular illumination area of diameter of about 5 mm.

The samples were analyzed as dry powders placed inside a home-built optical chamber equipped with a fused silica optical window and gas inlet and outlet. The light emitted *via* PL by the illuminated samples was collected using a lens system and focused on the input slit of the detection spectrometer (Triax 320 Horiba, f = 320 mm effective focal length) *via* a multimode optical fiber. The PL light was dispersed *via* 150 grooves per mm grating and imaged on a thermoelectrically cooled CCD camera operating at −70 °C. A long-wave pass optical filter with a cutoff wavelength of 500 nm was used to block the excitation light and to avoid the detection of spurious fluorescence from the liquid waveguide. The measured intensities of the PL spectra were automatically divided by the excitation intensity, corrected for the spectral response of the overall optical system and divided by the integration time. The intensity data are provided in counts per second (cps) units.

The gaseous environment in the optical cell was regulated *via* a mass flow controller connected with certified cylinders of dry N_2 (99.9995% purity), dry air (20% O_2 and 80% N_2) and ethanol/N_2 mixture (100 ppm EtOH concentration in N_2). The total flow through an entire experiment was always kept constant at a rate of 300 standard cubic centimeters per minute (sccm). All measurements were performed at room temperature.

2.3.3. Measurement protocol. Measurements in a controlled gaseous environment were performed in accordance with the following protocol. First, each sample, in the form of dry powders, was placed in an optical test chamber. The chamber was then closed, and a 300 sccm (standard cubic

centimeters per minute) flow of N_2 was activated. During the N_2 flow, the PL emission spectra of the samples were obtained by supragap excitation (illumination wavelength λ_{exc} = 364 nm) were monitored, tracking changes to the removal of O_2 and determining when a stable PL intensity was reached. As the PL signal stabilized in the N_2 atmosphere, a PLE map, defined in Subsection 3.2, was acquired ("PLE in N_2"). Successively, the gaseous environment was changed by stopping the N_2 flow and activating a 300 sccm flow of EtOH (at a concentration of 100 ppm, diluted in N_2). Throughout this transition, the PL emission under λ_{exc} = 364 nm illumination was continuously monitored until the PL stabilized in the new gaseous environment. Once a stable PL intensity in the EtOH environment was reached, another PLE map was performed ("PLE in EtOH"). Next, the EtOH flow was stopped and replaced by a 300 sccm flow of dry air from a certified bottle while again monitoring the PL emission using 364 nm excitation, as conducted previously. Finally, a last PLE map was acquired once the PL intensity was stabilized in dry air ("PLE in dry air").

It is noteworthy that the samples were continuously exposed to controlled gaseous at the same flow (300 sccm) once loaded into the cell and that all measurements were performed at room temperature. We chose to monitor the PL signal at λ_{exc} = 364 nm, as it is optimal for the excitation of the infrared PL, which exhibited fast and remarkably sensitive dynamics toward the gaseous species. We also underline that the powders were kept in the dark while stabilizing in different gaseous environments, except for the time interval when the PL spectra were monitored. Such illumination durations were set at 3 s for the B-AS sample and 6 s for the B700, as it exhibited less intense PL.

3. Results and discussion

3.1. Sample characterizations

TEM and HRTEM micrographs of the as-synthesized (B-AS) nanorods are reported in Fig. 1A and B, respectively. It is observed that hydrothermal synthesis leads to the formation of anisotropic nanostructures exhibiting well-defined shapes and exposed crystal facets. The TEM and HRTEM images shown in Fig. 1C and D refer to the sample thermally treated for 2 hours in hydrogen at temperature T = 700 °C (B700-2 h). Consistent with previous investigations, it is observed that the reduction process induces a partial reshaping of the nanostructures, leading to more irregular and isotropic nanoparticles. XRD analysis reported in ESI (Fig. S1†) for the synthesized nanorods evidence the characteristic XRD of (121) planes of brookite at $2q$ = 30°. It is important to note the absence of a diffraction peak at 32°, which is associated with the (110) plane of rutile TiO_2.

The analysis of B700 samples reported in our previous works[24] reveals that the nanorods remain stable, maintaining the brookite phase, while employing temperatures higher than 700 °C produced mainly the rutile phase (T = 800 °C) or the Magneli sub-oxide phase Ti_9O_{17}.

Raman analysis is highly effective in combination with XRD to verify the purity of the obtained brookite TiO_2. Anatase and rutile, being more symmetric than brookite, yield relatively simple Raman spectra featuring few active modes.[36] The less symmetric orthorhombic brookite yields many more bands than the other two polymorphs so that even small amounts of brookite TiO_2 can be detected in mixed-phase samples.[37] The Raman spectrum of B-AS and B700-2 h samples are reported in Fig. 1E, revealing the presence of the Raman-active mode characteristics for the brookite phase. It is to be noted that both the spectra shown in Fig. 1E show no Raman signal associated with the A_{1g} (~612 cm^{-1}) and E_g (~447 cm^{-1}) mode characteristics for the rutile phase. Hence, the Raman investigation further reinforces the evidence that the obtained brookite phase is pure and stable up to a processing temperature of 700 °C with no significant amount of rutile and anatase.

The Kubelka–Munk (KM) function for B-AS, B700-1 h and B700-2 h samples, obtained from the measured diffused reflectance spectra, are shown in Fig. 1F. The KM function $F(R)$ is determined according to the standard definition $F(\lambda) = (1 - R(\lambda))^2/2R(\lambda)$, where $R(\lambda)$ is the diffused reflectance of the material at wavelength l. As expected, the KM function for stoichiometric brookite B-AS is spectrally flat and has low values over the entire visible and near-infrared range. This indicates a diffused reflectance of $R(\lambda) \approx 1$ that is spectrally uniform over the entire visible range, which is consistent with the white appearance of the brookite powder.

It is clearly observed that the reductive treatment induced the formation of an optical absorption band with increased intensity at a longer wavelength and extended up to the near-infrared range (1100 nm and above), explaining the blueish/grey appearance of the reduced samples. The same modification of the absorption spectrum, leading to "blue titania", is found through other reductive means usually associated with milder reduction treatments.[23]

The new absorption band acquired from the reductive treatment is associated with a new optical transition with initial state electrons trapped at point defects created by the reductive process and conduction band states as final states.[38] At the present day, it is quite well agreed that the formation of a new defect-related optical absorption band does not necessarily coincide with an enhancement in visible light-activated photoactivity of the reduced sample. For example, experiments conducted on platinized reduced brookite nanorods show no improvement in the rate of H_2 production rate under visible light irradiation for reduced samples.[24]

3.2. PLE in a controlled environment: as-synthesized brookite nanorods

The intensity maps $\Phi(\lambda_{PL}\lambda_{exc})$ for B-AS samples are depicted in Fig. 2 as contour plots. The maps in Fig. 2A–C refer to B-AS in N_2, EtOH (100 ppm) and dry air, respectively. We refer to the data in Fig. 2A recorded in the inert N_2 environment as the "intrinsic" (i.e., adsorbate independent) PL emission of the B-AS.
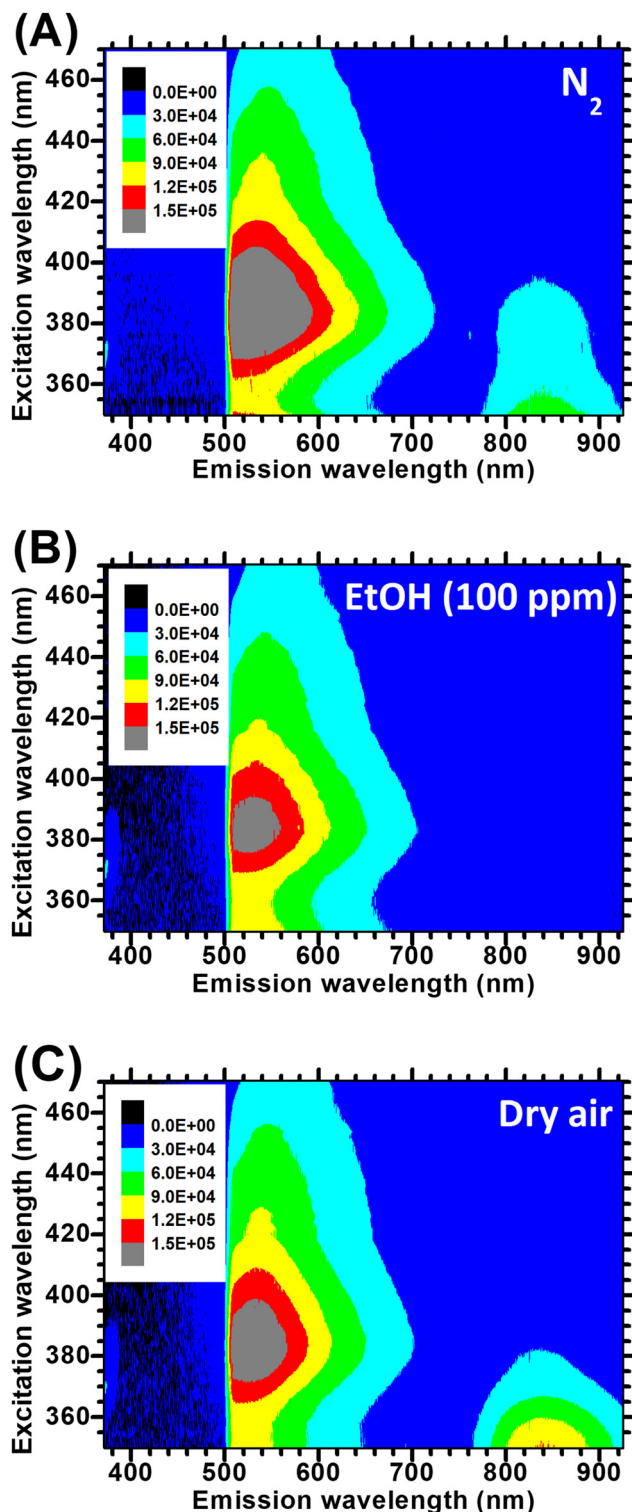
Fig. 2 PLE maps of as-synthesized brookite (B-AS), measured in N_2 (A), EtOH 100 ppm (B) and dry air (C) according to the experimental protocol described in section 2.4. The PL intensities are normalized by the exposure time and are thus expressed in counts per second (cps) units.

The main experimental findings inferable from the data in Fig. 2 can be summarized as follows:

(a) Simultaneous presence of a visible and near-infrared PL band.

(b) Significant PL activity in the visible range even at subgap excitation.

(c) PL-quenching effect operated by EtOH, mild on VIS-PL and strong for NIR-PL.

(d) Significant effect operated by O_2 exposure (N_2 vs. dry air PLE)

We expand on these points.

As mentioned in point (a) above, the data show that the PL spectra of B-AS NRs *always exhibit two components*, independent of the gaseous environment and the excitation wavelength tested. The first component is a broader one, extending in the visible (VIS) range and peaking at about 540 nm (~2.3 eV). The second is narrower, peaks at about 820 nm (1.51 eV), and extends in the 800–900 nm wavelength (1.55–1.37 eV) near-infrared interval. The two bands are hereinafter referred to as VIS-PL and NIR-PL. They resemble the PL characteristics exhibited by anatase (showing VIS-PL only) and rutile (NIR-PL only). Mixtures containing both phases, resulting from incomplete thermal conversion of anatase to rutile, also exhibit both PL bands.[39,40] However, brookite appears to be the only pure TiO_2 phase that shows the two bands simultaneously.

Additionally, we note that *both the supragap and subgap generate VIS-PL emission*. This occurs not just for the "intrinsic" PL intensity shown in Fig. 2B but also for all of the other examined gaseous environments. The situation is quite different for the other band: *NIR-PL is relevant only for supragap excitation*, except for a weak residual "tail" in the excitation range of 380–420 nm (this "tail" is better evidenced by the excitation spectra shown in Fig. 3). Moreover, *NIR-PL is strongly suppressed by exposure to EtOH* molecules, but this does not occur for VIS-PL.

The effect of EtOH exposure, mentioned in point (c), is quite relevant for NIR-PL, which is completely suppressed after inserting the EtOH flow. The complete quenching of NIR-PL occurs at all the excitation wavelengths (see Fig. 2B) and is fast, as the NIR-PL becomes unobservable within few minutes. Notably, EtOH quenches the VIS-PL, but in this case, the effect is milder. Additionally, no EtOH-related effect on PL intensity is observed when the excitation energy is well below the bandgap energy. This is more clearly recognizable by the observation of the excitation spectra reported (Fig. 3, excitation wavelengths longer than 420 nm).

Finally, a substantial impact is noted due to O_2 exposure (Fig. 2C), showing a clear O_2-induced decrease in the VIS-PL intensity and an increase in the NIR-PL. This highlights the dual role of O_2 as a quencher for VIS and enhancer for NIR bands in brookite, a fact that is known to occur separately for anatase and rutile phases of TiO_2.[41–44] It is, therefore, natural to infer that the similar charge recombination pathways are at play in all of the TiO_2 polymorphs.

The information contained in the PLE maps can be more easily visualized and deducted by plotting the excitation
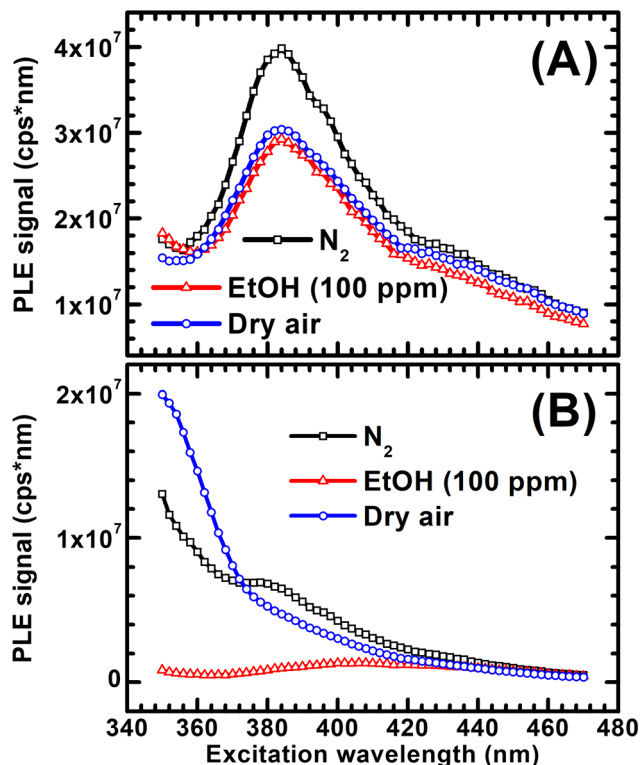
Fig. 3 Excitation spectra for B-AS calculated according to eqn (1) from the PLE map data in various gaseous environments. (A) Excitation spectra of the VIS-PL, calculated using the integration interval $\Delta\lambda_{PL}$ = 530–690 nm. (B) Excitation spectra of the NIR-PL, calculated using the integration interval $\Delta\lambda_{PL}$ = 800–900 nm. The black, red, and blue curves refer to the as-synthesized brookite nanorods in N_2, EtOH (100 ppm) and dry air.

spectra $I_{PLE}(\lambda_{exc})$ defined in eqn (1). They are shown in Fig. 3 as obtained from the data depicted in Fig. 2 and using the integration intervals $\Delta\lambda_{PL}$ = 530–690 nm (2.34–1.80 eV) to evaluate the total VIS-PL and $\Delta\lambda_{PL}$ = 800–900 nm (1.55–1.80 eV) for the total NIR-PL.

Regarding the NIR-PL (Fig. 3B), the excitation spectra are helpful in visualizing the complete suppression of NIR-PL caused by EtOH adsorption (black $vs.$ red curves) at all meaningful examined excitation wavelengths. Plot 3B also demonstrates that the shape of the excitation spectrum of O_2-enhanced NIR-PL in air resembles that of an interband absorption, with a slope change close to the nominal bandgap position ($\approx$370 nm). We also note that the O_2-induced enhance-

The excitation spectra for VIS-PL (Fig. 3A) clearly show that this band is quenched by O_2 compared to the intrinsic emission in N_2 (black $vs.$ blue curves), in particular for excitation energies close to the bandgap edge (*e.g.*, 360–400 nm excitation range). Moreover, O_2 is ineffective for PL excited by low energy (*i.e.*, λ_{exc} > 420 nm) photons, as the black and blue curves nearly perfectly overlap in this excitation range. Similarly, EtOH is a quencher for the VIS-PL in the entire spectrum of examined excitation wavelengths although the effect is very mild at longer wavelengths.

ment of NIR-PL is observed only for supragap excitation. This evidence proves insightful, as discussed later.

3.3. Recombination processes and PL mechanisms in as-synthesized brookites

The present discussion uses the symbols e_{CB}^- and h_{VB}^+ to denote the free (conduction band) electrons and (valence band) holes, respectively, while e_{tr}^- and h_{tr}^+ denote electrons and holes trapped at mid-gap states, respectively. As expected from the indirect nature of the TiO_2 bandgap, no band-to-band radiative recombination is observed. Hence, radiative recombination necessarily involves at least one carrier trapped in a mid-gap defective state in processes usually referred to as "free-to-bound" radiative recombination (FBRR) in the literature. This explains why the PL of TiO_2 is controlled by its defectivity and is the primary reason why PL studies are important in indirect-gap metal oxide photocatalysts.

For the sake of clarity, the PL mechanisms and charge recombination processes relative to the two observed emission bands are discussed separately.

3.3.1. VIS-PL in as-synthesized brookite. Based on the analysis of the experimental evidence, *we propose that the dominant mechanism for VIS-PL is the electron FBRR*, or, more precisely, the recombination of free or shallowly trapped electrons with deeply trapped holes formed through the relaxation of photogenerated free holes. A key factor in this process is the binding energy of the electrons (*i.e.*, their energetic distance from the conduction band edge), as the subgap excitation data suggest that the new electron states can be populated even 0.3 eV below the CB edge.

To explain how our proposal is deduced, we point out four pieces of evidence highlighted by the experimental results.

3.3.1.1. Spectral shape and peak position of the VIS-PL. As already noted, the PLE maps consistently show in all atmosphere environments that the VIS-PL is spectrally broad. This correlates positively with the broad distribution of (mid-gap) hole states suggested by quantum calculations and evidenced by photoemission data in the work by Hejazi *et al.*[24] The contrast with the spectral narrowness of NIR-PL is considered in the subsequent discussion.

3.3.1.2. VIS-PL quenching effect of O_2 at supragap excitation. Investigations conducted on anatase[43,45–49] have suggested that VIS-PL quenching specifically relates to a process involving free electrons e_{CB}^-. In particular, it originates from the scavenging of photogenerated free electrons by chemisorbed O_2, causing the formation of oxygen species with a charged character (*e.g.*, O_2^-, O^-) and consequent formation and enlargement of a depletion layer beneath the semiconductor surface.[50–52] As the depletion layer widens, the PL active region shrinks. Furthermore, O_2 scavenges electrons that could contribute to PL emission. The combination of the two effects (electron scavenging and depletion layer widening) mutually reinforces the PL quenching. This interpretation for the PL quenching is nowadays widely accepted for anatase, and all the pieces of evidence shown so far suggest that it should be invoked for brookite as well. The logical inference is that O_2-

induced quenching VIS-PL in brookite occurs *via* the same mechanism so that the PL emission mostly originates from free electrons.

3.3.1.3. Scarce effect of O_2 on VIS-PL at subgap excitation. As shown previously, the excitation spectra indicate that the O_2 effect becomes less relevant as the excitation photon energy falls below the bandgap threshold. This observation aligns with two contributing factors: (i) the reduced capacity of O_2 to scavenge deeply trapped electrons and (ii) the larger penetration depth of longer wavelength excitation. The latter implies the photogeneration of electrons deeper within the bulk, thus having a lower likelihood of migrating to the surface instead of recombining or being trapped before reaching it.

3.3.1.4. "Mild" quenching of VIS-PL induced by EtOH at all excitation wavelengths. Here, the term "mild" is not meant in the absolute sense, but in comparison to the much more drastic effect exerted by EtOH on the NIR-PL. Given the well-known ability of EtOH to scavenge the free holes in TiO_2, a logical way to interpret a PL quenching caused by EtOH is by proposing that valence band holes are involved in the VIS-PL. Free holes might either directly participate in the recombination or influence it indirectly by relaxing into trapped holes that then recombine in the FBRR process with free electrons. Either way, hole scavenging causes PL quenching.

It is very evident that ethanol's ability to quench VIS emission is significantly less than its ability to entirely suppress the NIR emission. This suggests that in VIS-PL, the valence band holes might not be directly involved in recombining with electrons. Instead, the VIS emission band likely involves holes that first transition (*i.e.*, relax) to trapped states and then undergo radiative recombination with electrons.

A scheme that sums up all the observations made so far for the VIS-PL and includes both the case of supragap (top figure) and subgap excitation (bottom figure) is shown in Fig. 4.

The blue vertical arrows indicate the optical absorption transitions of the electrons. The transition (a) in the upper figure represents an interband transition occurring by supragap excitation, while the transitions (d) and (e) in the lower figure indicate a subgap transition that generates free holes (represented by the empty circles) and shallowly trapped electrons (indicated by e_s^-) energetically positioned below the CBE edge. It is worth noting that these shallow states are likely the ones probed *via* transient absorption spectroscopy by Vequizo and coworkers, who found a fast relaxation kinetics of conduction band electrons towards these states and argued that the comparatively small energy depth of such states in brookite TiO_2 is optimal to improve the photocatalytic efficiency of brookite TiO_2 compared to the rutile phase.[13]

The colored region above the valence band edge (VBE) represents a broad distribution of initially occupied mid-gap states, previously evidenced in the as-synthesized brookite NRs and attributed to TiO_6 octahedra deformations.[24] After photogeneration, the charge carriers undergo fast relaxation toward states with lower energy for electrons and higher energy for
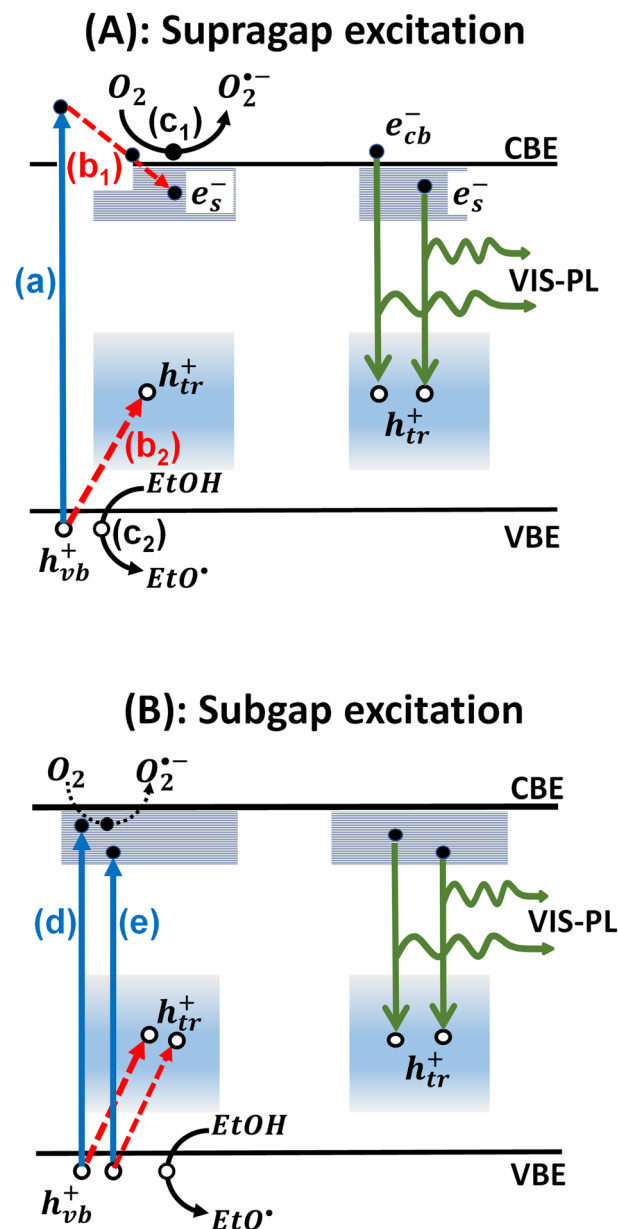

Fig. 4 Proposed scheme for the VIS-PL of brookite nanorods. Supragap optical absorption, indicated by (a) in the top figure, generates free carriers that can relax to the available states of interaction with O_2 and EtOH. The relaxations are indicated by dashed arrows and labelled as (b1) for electrons and (b2) for holes. Electron scavenging by O_2 and hole scavenging by EtOH are labelled by (c1) and (c2), respectively. As demonstrated by the observed VIS-PL emission at subgap excitation, optical transitions can also occur at lower excitation energies, populating available levels below the conduction band edge (CBE), as indicated by labels (d) and (e) in the bottom figure. Lower energy excited electrons are less prone to reaction with adsorbed O_2: this is represented by the use of a thinner dashed line for capture of electrons excited by transition (d). Finally, the relaxed photogenerated electrons remaining in the conduction band (e_{cb}^-) or in subgap shallow states (e_s^-) can recombine with relaxed trapped holes (h_{tr}^+).

holes, represented in the figure by diagonal dashed red lines. In particular, (b1) and (b2) label an electron and hole relaxation, respectively.

In Fig. 4, the capture of relaxing charge carriers by oxidizing or reducing molecules is represented through processes labelled as (c_1) (oxidation by O_2) and (c_2) (reduction by EtOH). Conduction band electrons able to migrate to the surface can interact with O_2, forming charged species and quenching the PL. This quenching is expected to be less effective for electrons excited in subgap shallow states (as shown in (d) and (e)) due to their higher binding energy and the larger optical penetration depth of the long wavelength excitation. This fact is pictured symbolically using a thinner dashed line for the $O_2^{\bullet-}$ formation.

As the relaxation is completed, PL occurs by radiative recombination processes indicated by the green arrows directed downwards. Based on the consideration made so far, photon emission is expected to occur *via* the radiative recombination of free or weakly bounded electrons with trapped holes populating the mid-gap states. The large energy dispersion of the mid-gap states can account for the spectrally broad VIS-PL.

It is noteworthy that the mechanism shown in Fig. 4 provides an interpretation of the observed mild quenching caused by EtOH across all involved excitation wavelengths. In fact, in this scheme, all the radiative transitions involve trapped holes h_{tr}^+, resulting from the relaxation of photogenerated free holes h_{vb}^+. Such relaxation is always in competition with the scavenging of free holes by EtOH.

3.3.2. NIR-PL in as-synthesized brookite.
The experimental findings indicate that the brookite NIR-PL does not originate from the same processes that cause its VIS-PL. This is evidenced by the fact that O_2 acts as an enhancer of NIR-PL at supragap excitation, while the exact opposite occurs for VIS-PL. Another point to consider is that EtOH is significantly more efficient at quenching NIR-PL than VIS-PL. According to these facts, we can derive the following points:

(1) NIR-PL cannot originate from free and/or shallowly bounded electrons that contribute to VIS-PL (see the scheme in Fig. 4). Therefore, NIR-PL must involve deeply trapped electrons (e_{tr}^-) with energies low enough to avoid being scavenged by O_2.

(2) According to the established mechanisms of electron scavenging by O_2, the NIR-PL enhancing activity of O_2 strongly suggests the involvement of free holes h_{VB}^+. In fact, the formation of charged species (*e.g.*, O_2^-) at the surface resulting from electron scavenging implies an increase in the density of free holes h_{VB}^+ in the sub-surface region. This, in turn, implies an increased spatial overlap of free holes with low-energy electrons trapped in the vicinity of the surface and, hence, an improved probability of their radiative recombination.

We sum up these observations by proposing a mechanism in which the NIR-PL occurs *via* radiative recombination of deeply trapped electrons e_{dt}^- positioned at about half of the bandgap with photogenerated free holes. It is worth noting that these trapped electrons have to be non-photogenerated (that is, the associated deep energy levels are not occupied *via* the relaxation of photogenerated electrons from the conduction band). Otherwise, O_2 would function as a PL quencher, as in the case of VIS-PL. A similar mechanism is proposed for the

origin of PL emission in rutile TiO_2,[43,53] which suggests that similar kinds of defects are also involved in the brookite phase.

The PL analysis alone cannot provide the exact chemical nature of the mentioned deep defects, but it allows some considerations based on the PL energy peak position and spectral width. We note that the NIR-PL spectra are narrow in energy (much narrower compared to the VIS one) and are peaked at about 830 nm, corresponding to about 1.49 eV. This indicates that the involved energy levels are very deep and positioned at about half of the bandgap region. The narrow energy distribution of these electron traps and their energy depth suggest that they are associated with very localized point defects. Recalling that radiative free-to-bound recombination requires electron/hole spatial overlapping, we suggest attributing the trapping states to surface point defects and/or to defects localized just at the subsurface layers.

Another factor supporting the surface nature of the NIR-PL is the observation of the radical difference in the efficiency of PL quenching by ethanol when considering the NIR emission (complete suppression) *vs.* the VIS one (mild suppression). It is well known that EtOH efficiently scavenges holes close to the catalyst surface. According to our observations, VIS-PL emission involves both surface and non-surface (free) holes. Thus, the scavenging activity of surface-adsorbed EtOH produces only partial quenching of the VIS-PL emission. Moreover, the assumption that NIR-PL occurs at surface states explains why EtOH is much more effective on this PL band.

The overall mechanism is presented in Fig. 5. The left panel in Fig. 5A shows the situation in which the sample is photoexcited in an inert environment (*i.e.*, N_2). Assuming for the sake of simplicity that no significant surface charge is developed, *i.e.*, the band edges are flat, the free electrons and holes are spread uniformly in the bulk of the nanocrystal. The electrons at deep traps close to the surface are indicated as e_{dt}^-. Holes in the bulk of the nanocrystal can participate in VIS-PL, as indicated previously, while NIR-PL occurs by involving the trapped holes close to the surface *via* radiative recombination $e_{dt}^- + h_{VB}^+ \rightarrow$ NIR-PL. It is worth mentioning that interstitial Ti atoms are proposed[54] as possible surface sites of electron traps in rutile TiO_2 although no definitive conclusion can be outlined in our case.

The effect of adsorbed O_2 and EtOH is shown in the right panel (Fig. 5B), which depicts the near-surface accumulation of free holes in an oxygen environment as the chemisorbed superoxide radicals $(O_2^{\bullet-})$ are developed. The hypothesis that NIR emission occurs as a surface phenomenon also explains why the PL-quenching activity of ethanol is more efficient for the NIR emission, considering that the scavenging of free holes by chemisorbed ethanol is more efficient close to the surface.

The NIR-PL occurring *via* surface-localized mechanisms is reflected by its fast responsivity to EtOH adsorption. An example is shown in Fig. 6, demonstrating the time dynamics of the total NIR-PL intensity excited at 364 nm, as monitored between the changes in the gaseous composition in the
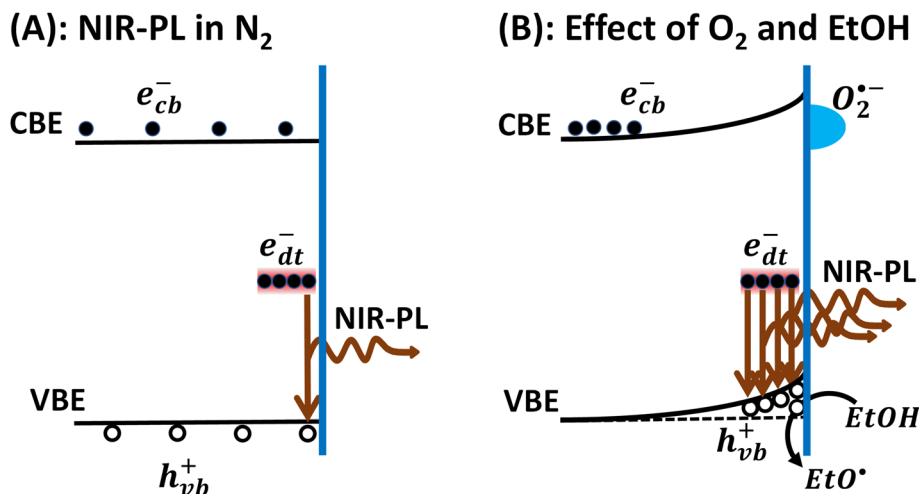
Fig. 5 (A) Proposed scheme for the intrinsic NIR-PL of brookite when the photoexcited sample is in an inert environment. Native (*i.e.*, non-photo-generated) deeply trapped mid-gap electronic states are indicated as e_{dt}^-, whose radiative transitions are proposed to cause the NIR-PL emission. In the figure, the empty and full circles indicate photogenerated holes and electrons, respectively. (B) Modification of the scheme when the sample is photoexcited in an O_2 or EtOH environment. The NIR-PL enhancement is explained in terms of the development of $O_2^{\bullet-}$ species, with consequent band bending and accumulation of free holes. The efficiency of NIR-PL suppression by EtOH is interpreted due to the surface localization of the radiative recombination processes.
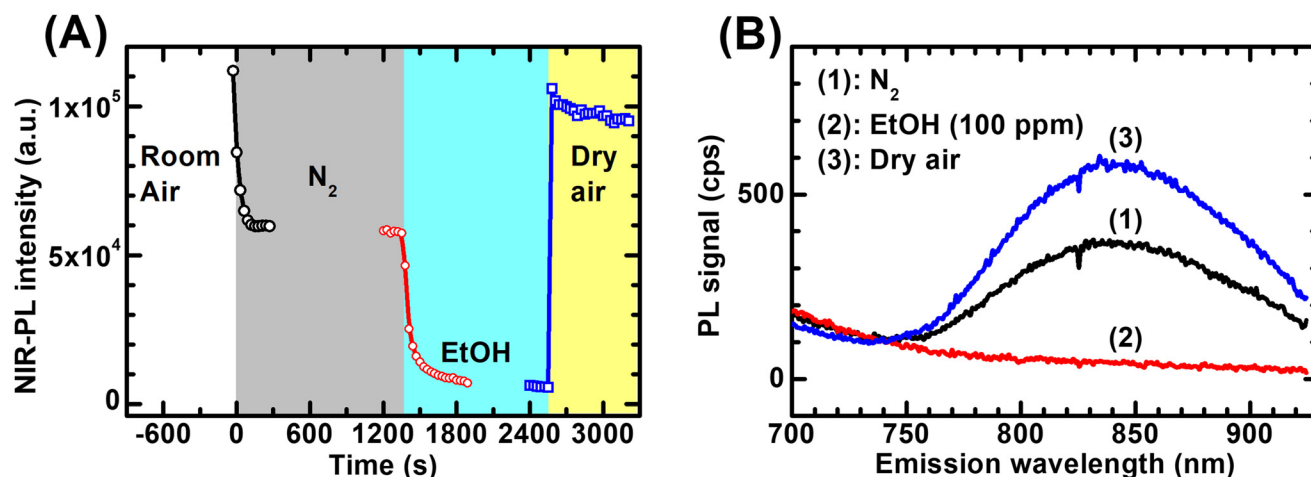

Fig. 6 (A) Total NIR-PL intensity at excitation wavelength λ_{exc} = 364 nm of B-AS nanorods during exposure to different gaseous species. (B) NIR-PL spectra of B-AS measured in different gaseous environments under stabilized conditions. (1, black curve): NIR-PL curve after 5 min exposure to N_2, (2, red curve): NIR-PL curve after 8 min exposure to EtOH (100 ppm in N_2), and (3, blue curve): NIR-PL curve after 8 min exposure to dry air.

measurement chamber (Fig. 6A). The NIR-PL spectra corresponding to stabilized conditions in the different environments are depicted in Fig. 6B.

3.4. PLE in a controlled environment of reduced brookite nanorods

The PLE analyses are conducted on thermally treated brookite NRs treated at 700 °C (B700) for different time durations (1 hour and 2 hours) by employing the same experimental procedure described for the as-prepared samples. The data for B700-2 h are presented in Fig. 7 (PLE maps) and Fig. 8 (exci-

tation spectra), while those for B700-1 h, which led to qualitatively equivalent results, are reported in the ESI (Fig. S3†).

Fig. 7 shows the PLE maps obtained for B700-2 h in N_2 (Fig. 7A), EtOH 100 ppm (Fig. 7B) and in dry air (Fig. 7C). In Fig. 8, we report the corresponding excitation spectra for the two PL bands of B700-2 h. These spectra were obtained using the same emission wavelength intervals as those employed to extract the data relative to the as-prepared samples depicted in Fig. 3.

Some of the findings evidenced in Fig. 7 are qualitatively equivalent to those obtained for the B-AS nanorods. In particular, we again observe two emission bands (VIS and NIR) and a
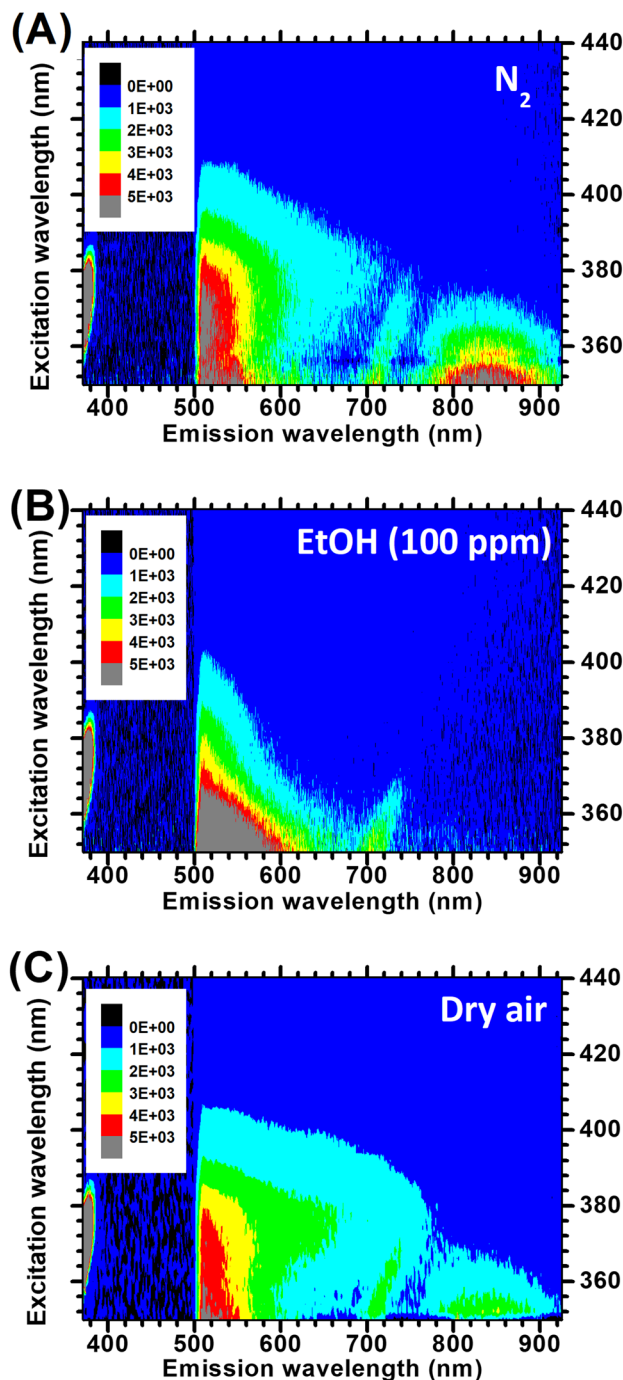
Fig. 7 PLE maps of the B700-2 h sample measured in N$_2$ (A), EtOH 100 ppm (B) and dry air after exposure to EtOH (C). PL intensities are reported in cps units. The data are acquired *via* the same experimental procedure as those in Fig. 2.

Fig. 8 (A) Excitation spectra of the VIS–PL band B700-2 h calculated using the integration interval $\Delta\lambda_{PL}$ = 530–690 nm. (B) Excitation spectra of the NIR–PL band of B700-2 h calculated using the integration interval $\Delta\lambda_{PL}$ = 800–900 nm. The black, red, and blue curves refer to the sample in N$_2$, EtOH (100 ppm) and dry air, respectively. All the curves are obtained using the PLE maps shown in Fig. 6.

strong EtOH-induced quenching of NIR-PL. Such findings are already observed in the stoichiometric brookite nanorods and discussed in the previous section.

Moreover, three significant peculiarities of the reduced samples are easily recognizable.

1. The PL intensity for the reduced brookite is much lower than that for the B-AS sample.
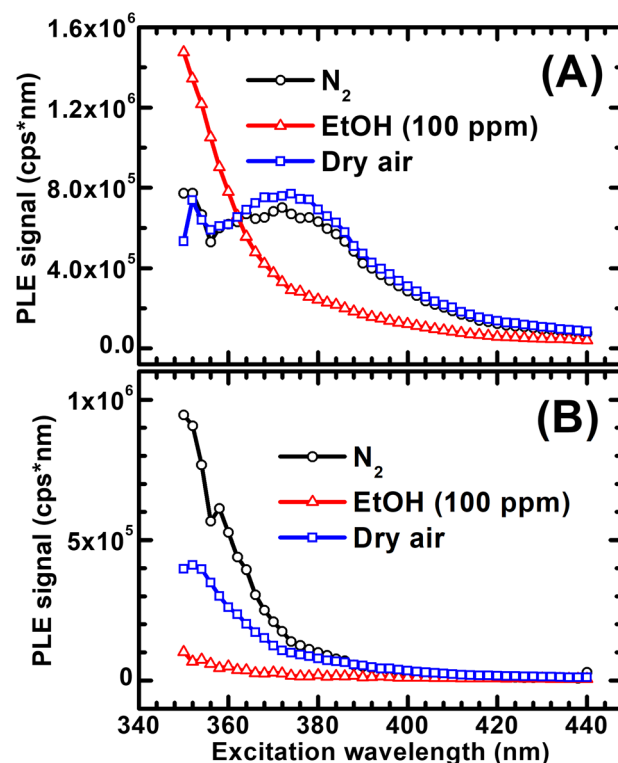
2. Compared to B-AS, a lesser PL quenching effect induced by O$_2$ is observed.

3. EtOH not only removes the NIR-PL (as already observed for untreated B-AS NRs) but also peculiarly affects the VIS-PL. It causes a quenching for excitation below the bandgap edge (consistently with what was observed in B-AS) and a surprising enhancement for excitation photon energy E > 3.45 eV (excitation wavelength shorter than 360 nm), which was not observed in the untreated B-AS samples.

The decrease in PL intensity is easier to interpret. It is known that the thermal treatment in H$_2$ enhances the density of defective mid-gap states and band-tail states *via* lattice distortion and oxygen vacancies.[24] These defects typically function as non-radiative recombination centers, lowering the PL intensity.

The other two effects indicate that the interactions of the reduced brookite with the gaseous species are quite different from those observed in the B-AS samples. Their interpretation is more challenging.

Regarding the minor effect of O$_2$ on the PL intensity of B700-2 h NRs, it is worth mentioning that significant differences in how O$_2$ influences the PL of anatase TiO$_2$ have been reported previously[40,44,55] and interpreted as a morphology-dependent effect. More precisely, although VIS-PL quenching

induced by O_2 has been repeatedly observed in P25 TiO_2,[40,41] isotropic anatase TiO_2 nanoparticles[52,55,56] and other metal oxides,[46,50,57] the case of anatase PL unaffected by O_2 exposure has been reported for the as-prepared nanosheets of anatase TiO_2 predominantly that expose (001) crystal facets.[44] To explain this experimental finding, Mercado and coworkers[44] tentatively invoked differences in the formation energy of oxygen vacancies and, therefore, differences in reactivity toward O_2 of the distinct crystal facets.

In our case, the interpretation in terms of the surface reactivity of the minor PL response of the reduced sample to O_2 would be misleading. The surface properties of the reduced and the as-synthesized NRs are radically different: B700 is intentionally reduced and does not expose well-defined crystal facets (Fig. S1†), while B-AS is stoichiometric and shows defined crystal facets.[58]
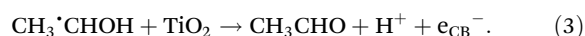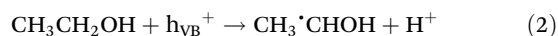
Instead, we point out that the evidence suggests that the O_2-induced PL quenching occurs *via* the scavenging of photogenerated electrons. Such a process can only occur after the photogenerated electrons reach the nanorod surface where adsorbed O_2 is present. Compared to the B-AS, the reduced samples exhibit larger concentrations of point defects. This implies a hindered mobility of free charge carriers and thus a lower probability that mobile charges will reach the surface, and hence a lower number of PL-quenching electron scavenging events. This looks like a natural explanation of why, compared to B-AS, a lesser PL quenching effect induced by O_2 is observed in the reduced brookite.

The EtOH-induced increase in VIS-PL at supragap excitation is probably the most peculiar and interesting experimental result among those listed thus far. Its relevance lies in the fact that, as subsequently discussed, it can be the manifestation of the substrate-specific process occurring during the photo-oxidation of alcohols on the reduced brookite, which is one of the main purposes of this work.

It is easily noticeable that such an effect occurs only for the VIS-PL at supragap excitation, as easily shown by comparing the black and red curves in Fig. 8A. For subgap excitation, we obtain the same PL quenching already observed for untreated B-AS nanorods. Moreover, the effect does not occur for the NIR-PL.

We recall that in our interpretation (Fig. 4), the VIS-PL at supragap excitation originates from the recombination of conduction band electrons. Hence, the EtOH-induced enhancement of VIS-PL suggests that the interaction of ethanol with the reduced NRs causes an increase in the density of conduction band electrons. This leads us to invoke a known effect occurring in photooxidation of different alcohols by TiO_2 photoanodes, namely the "current doubling" effect, manifesting as anodic currents larger than the oxidative hole current and caused by the injection of electrons from transient radical species of oxidized alcohols into the conduction band of the TiO_2.[59–61] Importantly, the effect is not observed for electrodes made of undoped TiO_2[59,60] but is evidenced when TiO_2 is compounded with MoO_2 and MoS_2 cocatalysts and when it is intentionally doped with donor defects.[60]

In accordance with already established evidence for photo-oxidation of methanol on anatase TiO_2,[61] we propose that the free electron injection in thermally reduced brookite NRs occurs through initial oxidation of ethanol by photogenerated holes with the formation of $CH_3{}^{\bullet}CHOH$ radicals *via* hydrogen abstraction from the carbon atom of ethanol (eqn (2)), followed by electron injection and further hydrogen abstraction from the –OH group (eqn (3)), *i.e.*:

$$CH_3CH_2OH + h_{VB}{}^+ \rightarrow CH_3{}^{\bullet}CHOH + H^+ \quad (2)$$

$$CH_3{}^{\bullet}CHOH + TiO_2 \rightarrow CH_3CHO + H^+ + e_{CB}{}^-. \quad (3)$$

Similar processes in the photooxidation of methanol leading to the formation of formaldehyde are documented by, for example, Kandiel and coworkers.[61] We recall that EtOH acts solely as a PL quencher on as-synthesized brookite (see Fig. 2 and 3) through hole scavenging. The observed EtOH-induced enhancement of PL in the reduced samples thus indicates alcohol photooxidation processes; for example, the one proposed here in eqn (2) and (3) are more efficient than hole scavenging.

It is worth noting that an ethanol-induced VIS-PL enhancement at supragap excitation is also observed for the B700-1 h samples (Fig. S3†). Therefore, there is a positive correlation between the reductive thermal treatment and the emergence of specific and dominant alcohol photooxidation processes, such as the aforementioned current doubling phenomenon, which we hypothesize to interpret the experimental results. Further experiments are required to test this hypothesis, which might help explain the evidence reported regarding the exceptional reactivity of reduced brookite NRs toward the photo-oxidation of alcohols and the related efficiency of photocatalytic hydrogen generation.

As a final note, we point out that the PL enhancement caused by EtOH at supragap illumination is more pronounced for PL components with shorter wavelengths. This can be observed by inspecting the map of Fig. 7C and by noticing that, compared to the data in Fig. 6B, the VIS-PL increases predominantly in the emission wavelength interval of 500–600 nm.

To better support this interesting point, we show in the ESI† the calculated excitation spectra that correspond to different sub-intervals of the total VIS-PL emission. More precisely, Fig. S4† shows the total PL intensity emitted as higher-energy "green" light (emission intervals of 530–580 nm) and as lower-energy "red" light (640–690 nm) in the various gaseous environments. The data show that for supragap excitation, the EtOH-induced enhancement of PL intensity in B700 acts more relevantly on the "green" part of the PL spectrum (Fig. S4 and S5†). This suggests, based on the interpretation we gave on the causes of EtOH-induced PL enhancement, that the recombination of free electrons with trapped holes is mainly associated with the higher-energy components of the PL spectra.

4. Conclusions

In the present work, we used PLE spectroscopy in controlled environment and carried out a study involving the excitation of sub-bandgap states under successive exposures to a reducing (ethanol) and oxidizing (oxygen) species to provide a picture of the various charge-carrier recombination processes occurring in pristine and reduced TiO_2 brookite nanorods.

Based on the experimental findings, we deduced an interpretation model describing the main charge recombination processes and PL mechanisms, including information about the spatial and energetic positions of the intragap states involved. In more detail, based on the PL characteristics observed for both supragap and subgap excitation, and on their changes induced by exposure to the gaseous reactants, we propose that part of the photogenerated holes are spontaneously trapped to gap states so that radiative recombination of free and shallowly trapped electrons recombining with these trapped holes leads to the visible PL band. Moreover, the near-infrared PL band stems from the recombination of free holes with non-photogenerated surface-trapped and deeply energetic electrons with free holes. These last processes likely occur at the nanorod surface and/or in near-surface layers, as suggested by both the analysis of the PLE data and the data recorded during the transition between different gaseous environments. This appears to be promising because of its applications in optochemical sensing.

Furthermore, we identified a substrate-specific effect occurring in the interaction between reduced brookite nanorods and ethanol, consisting of a large enhancement of visible PL at supragap excitation, which might be interpreted as electrons being injected into the conduction band of reduced brookite NRs via the initial oxidation of ethanol. Further investigations will be conducted on this phenomenon, which may shed more light on the empirical evidence reported regarding their exceptional reactivity toward the photo-oxidation of alcohols and the concomitant efficiency of photocatalytic hydrogen generation.

Author contributions

SL conceived the work. MHH and MS synthesized the samples and conducted the preliminary characterizations (X-ray diffraction, TEM, Raman, diffused reflectance). AF and SL prepared the experimental setup for PLE spectroscopy in controlled environment. RR conducted the PLE measurements, with contributions from SL and AF. SL conducted the data analysis. SL, MHH and AN wrote the manuscript, with contributions from AF, SK and PM. SL, AN, PM and SK supervised the activity. RR and AF contributed equally to the work. All authors have given approval to the definitive version of the manuscript.

Conflicts of interest

There are no conflicts to declare.

Acknowledgements

References

1 G. Žerjav, K. Žižek, J. Zavašnik and A. Pintar, *J. Environ. Chem. Eng.*, 2022, **10**, 107722.

2 R. Viter and I. Iatsunskyi, in *Nanomaterials Design for Sensing Applications*, Elsevier, 2019, pp. 41–91.

3 C. Zhang, G. Liu, X. Geng, K. Wu and M. Debliquy, *Sens. Actuators, A*, 2020, **309**, 112026.

4 O. Glemser and E. Schwarzmann, *Angew. Chem.*, 1956, **68**, 791–791.

5 M. Monai, T. Montini and P. Fornasiero, *Catalysts*, 2017, **7**, 304.

6 A. Di Paola, M. Bellardita and L. Palmisano, *Catalysts*, 2013, **3**, 36–73.

7 D. R. Eddy, M. D. Permana, L. K. Sakti, G. A. N. Sheha, Solihudin, S. Hidayat, T. Takei, N. Kumada and I. Rahayu, *Nanomaterials*, 2023, **13**, 704.

8 M. Manzoli, F. S. Freyria, N. Blangetti and B. Bonelli, *RSC Adv.*, 2022, **12**, 3322–3334.

9 J. Bao, H. Maimaiti, X. Zhao, J. Sun and L. Feng, *Appl. Surf. Sci.*, 2022, **602**, 154328.

10 C. Günnemann, C. Haisch, M. Fleisch, J. Schneider, A. V. Emeline and D. W. Bahnemann, *ACS Catal.*, 2019, **9**, 1001–1012.

11 M. Cargnello, T. Montini, S. Y. Smolin, J. B. Priebe, J. J. Delgado Jaén, V. V. T. Doan-Nguyen, I. S. McKay, J. A. Schwalbe, M.-M. Pohl, T. R. Gordon, Y. Lu, J. B. Baxter, A. Brückner, P. Fornasiero and C. B. Murray, *Proc. Natl. Acad. Sci. U. S. A.*, 2016, **113**, 3966–3971.

12 T. A. Kandiel, L. Robben, A. Alkaima and D. Bahnemann, *Photochem. Photobiol. Sci.*, 2013, **12**, 602–609.

13 J. J. M. Vequizo, H. Matsunaga, T. Ishiku, S. Kamimura, T. Ohno and A. Yamakata, *ACS Catal.*, 2017, **7**, 2644–2651.

14 M. Kamran, T. A. Kandiel, S. Abdel-Azeim, M. A. Morsy and D. W. Bahnemann, *J. Phys. Chem. C*, 2023, **127**, 7707–7717.

15 X. Li, J. Yu, M. Jaroniec and X. Chen, *Chem. Rev.*, 2019, 218.

16 A. Meng, L. Zhang, B. Cheng and J. Yu, *Adv. Mater.*, 2019, 1807660.

17 M. Pylarinou, A. Toumazatou, E. Sakellis, E. Xenogiannopoulou, S. Gardelis, N. Boukos, A. Dimoulas and V. Likodimos, *Materials*, 2021, **14**, 7117.

18 M.-A. Apostolaki, E. Sakellis, P. Tsipas, M. Giannouri, S. Gardelis, N. Boukos, A. Dimoulas and V. Likodimos, *Appl. Surf. Sci.*, 2023, **613**, 155919.

19 Y. Chen, S. Ji, C. Chen, Q. Peng, D. Wang and Y. Li, *Joule*, 2018, **2**, 1242–1264.

20 H. V. Thang, G. Pacchioni, L. DeRita and P. Christopher, *J. Catal.*, 2018, **367**, 104–114.

21 E. Wierzbicka, M. Altomare, M. Wu, N. Liu, T. Yokosawa, D. Fehn, S. Qin, K. Meyer, T. Unruh, E. Spiecker,

L. Palmisano, M. Bellardita, J. Will and P. Schmuki, *J. Mater. Chem. A*, 2021, **9**, 1168–1179.

22 X. Chen, L. Liu and F. Huang, *Chem. Soc. Rev.*, 2015, **44**, 1861–1885.

23 A. Naldoni, M. Altomare, G. Zoppellaro, N. Liu, Š. Kment, R. Zbořil and P. Schmuki, *ACS Catal.*, 2019, **9**, 345–364.

24 S. M. H. Hejazi, M. Shahrezaei, P. Błoński, M. Allieta, P. M. Sheverdyaeva, P. Moras, Z. Baďura, S. Kalytchuk, E. Mohammadi, R. Zbořil, Š. Kment, M. Otyepka, A. Naldoni and P. Fornasiero, *Chem. Catal.*, 2022, **2**, 1177–1190.

25 M. Anpo and M. Che, in *Advances in Catalysis*, Elsevier, 1999, vol. 44, pp. 119–257.

26 E. Comini, C. Baratto, I. Concina, G. Faglia, M. Falasconi, M. Ferroni, V. Galstyan, E. Gobbi, A. Ponzoni, A. Vomiero, D. Zappa, V. Sberveglieri and G. Sberveglieri, *Sens. Actuators, B*, 2013, **179**, 3–20.

27 M. Nasr, A. Abou Chaaya, N. Abboud, M. Bechelany, R. Viter, C. Eid, A. Khoury and P. Miele, *Superlattices Microstruct.*, 2015, **77**, 18–24.

28 M. Anpo, M. Tomonari and M. A. Fox, *J. Phys. Chem.*, 1989, **93**, 7300–7302.

29 G. Ambrosone, U. Coscia, S. Lettieri, P. Maddalena, C. Privato and S. Ferrero, *Thin Solid Films*, 2002, **403–404**, 349–353.

30 J. Liqiang, Q. Yichun, W. Baiqi, L. Shudan, J. Baojiang, Y. Libin, F. Wei, F. Honggang and S. Jiazhong, *Sol. Energy Mater. Sol. Cells*, 2006, **90**, 1773–1787.

31 L. Mascaretti, V. Russo, G. Zoppellaro, A. Lucotti, C. S. Casari, Š. Kment, A. Naldoni and A. Li Bassi, *J. Phys. Chem. C*, 2019, **123**, 11292–11303.

32 E. G. Barbagiovanni, R. Reitano, G. Franzò, V. Strano, A. Terrasi and S. Mirabella, *Nanoscale*, 2016, **8**, 995–1006.

33 S. Lettieri, V. Gargiulo, D. K. Pallotti, G. Vitiello, P. Maddalena, M. Alfè and R. Marotta, *Catal. Today*, 2018, **315**, 19–30.

34 F. Ehré, C. Labbé, C. Dufour, W. M. Jadwisienczak, J. Weimmerskirch-Aubatin, X. Portier, J.-L. Doualan, J. Cardin, A. L. Richard, D. C. Ingram, C. Labrugère and F. Gourbilleau, *Nanoscale*, 2018, **10**, 3823–3837.

35 E. H. Khan, M. H. Weber and M. D. McCluskey, *Phys. Rev. Lett.*, 2013, **111**, 017401.

36 P. P. Lottici, D. Bersani, M. Braghini and A. Montenero, *J. Mater. Sci.*, 1993, **28**, 177–183.

37 M. N. Iliev, V. G. Hadjiev and A. P. Litvinchuk, *Vib. Spectrosc.*, 2013, **64**, 148–152.

38 S. Lettieri, V. Gargiulo, M. Alfè, M. Amati, P. Zeller, V.-A. Maraloiu, F. Borbone, M. Pavone, A. B. Muñoz-García and P. Maddalena, *J. Phys. Chem. C*, 2020, **124**, 3564–3576.

39 A. Setaro, S. Lettieri, D. Diamare, P. Maddalena, C. Malagù, M. C. Carotta and G. Martinelli, *New J. Phys.*, 2008, **10**, 053030.

40 F. J. Knorr, C. C. Mercado and J. L. McHale, *J. Phys. Chem. C*, 2008, **112**, 12786–12794.

41 S. Ma, M. E. Reish, Z. Zhang, I. Harrison and J. T. Yates, *J. Phys. Chem. C*, 2017, **121**, 1263–1271.

42 S. Lettieri, D. K. Pallotti, F. Gesuele and P. Maddalena, *Appl. Phys. Lett.*, 2016, **109**, 031905.

43 D. K. Pallotti, S. Amoruso, E. Orabona, P. Maddalena and S. Lettieri, *Sens. Actuators, B*, 2015, **221**, 515–520.

44 C. C. Mercado, F. J. Knorr, J. L. McHale, S. M. Usmani, A. S. Ichimura and L. V. Saraf, *J. Phys. Chem. C*, 2012, **116**, 10796–10804.

45 R. E. Rex, F. J. Knorr and J. L. McHale, *J. Phys. Chem. C*, 2014, **118**, 16831–16841.

46 N. Siedl, D. Koller, A. K. Sternig, D. Thomele and O. Diwald, *Phys. Chem. Chem. Phys.*, 2014, **16**, 8339.

47 D. Pallotti, E. Orabona, S. Amoruso, P. Maddalena and S. Lettieri, *Appl. Phys. Lett.*, 2014, **105**, 031903.

48 A. Setaro, A. Bismuto, S. Lettieri, P. Maddalena, E. Comini, S. Bianchi, C. Baratto and G. Sberveglieri, *Sens. Actuators, B*, 2008, **130**, 391–395.

49 D. Valerini, A. Cretì, A. P. Caricato, M. Lomascolo, R. Rella and M. Martino, *Sens. Actuators, B*, 2010, **145**, 167–173.

50 S. Morandi, A. Fioravanti, G. Cerrato, S. Lettieri, M. Sacerdoti and M. C. Carotta, *Sens. Actuators, B*, 2017, **249**, 581–589.

51 A. Stevanovic and J. T. Yates, *J. Phys. Chem. C*, 2013, **117**, 24189–24195.

52 T. Berger, M. Sterrer, O. Diwald, E. Knözinger, D. Panayotov, T. L. Thompson and J. T. Yates, *J. Phys. Chem. B*, 2005, **109**, 6061–6068.

53 J. J. M. Vequizo, S. Kamimura, T. Ohno and A. Yamakata, *Phys. Chem. Chem. Phys.*, 2018, **20**, 3241–3248.

54 B. Santara, P. K. Giri, K. Imakita and M. Fujii, *J. Phys. Chem. C*, 2013, **117**, 23402–23411.

55 C. C. Mercado, F. J. Knorr and J. L. McHale, *ACS Nano*, 2012, **6**, 7270–7280.

56 M. Alfè, V. Gargiulo, M. Amati, V.-A. Maraloiu, P. Maddalena and S. Lettieri, *Catalysts*, 2021, **11**, 795.

57 A. R. Gheisi, C. Neygandhi, A. K. Sternig, E. Carrasco, H. Marbach, D. Thomele and O. Diwald, *Phys. Chem. Chem. Phys.*, 2014, **16**, 23922–23929.

58 A. Naldoni, T. Montini, F. Malara, M. M. Mróz, A. Beltram, T. Virgili, C. L. Boldrini, M. Marelli, I. Romero-Ocaña, J. J. Delgado, V. Dal Santo and P. Fornasiero, *ACS Catal.*, 2017, **7**, 1270–1278.

59 Y. Nosaka, H. Sasaki, K. Norimatsu and H. Miyama, *Chem. Phys. Lett.*, 1984, **105**, 456–458.

60 N. Hykaway, W. M. Sears, H. Morisaki and S. R. Morrison, *J. Phys. Chem.*, 1986, **90**, 6663–6667.

61 T. A. Kandiel, R. Dillert and D. W. Bahnemann, *Photochem. Photobiol. Sci.*, 2009, **8**, 683–690.